

Cite this: *J. Mater. Chem.*, 2011, **21**, 10077

www.rsc.org/materials

PAPER

Nanosheet-structured LiV_3O_8 with high capacity and excellent stability for high energy lithium batteries†

Anqiang Pan,^{ab} Ji-Guang Zhang,^{*b} Guozhong Cao,^c Shuquan Liang,^{*a} Chongmin Wang,^b Zimin Nie,^b Bruce W. Arey,^b Wu Xu,^b Dawei Liu,^c Jie Xiao,^b Guosheng Li^b and Jun Liu^{*b}

Received 7th March 2011, Accepted 13th April 2011

DOI: 10.1039/c1jm10976f

Highly stable LiV_3O_8 with a nanosheet-structure was successfully prepared using polyethylene glycol (PEG) polymer in the precursor solution as the structure modifying agent, followed by calcination in air at 400 °C, 450 °C, 500 °C, and 550 °C. These materials provide the best electrochemical performance ever reported for LiV_3O_8 crystalline electrodes, with a specific discharge capacity of 260 mAh g⁻¹ and no capacity fading over 100 cycles at 100 mA g⁻¹. The excellent cyclic stability and high specific discharge capacity of the material are attributed to the novel nanosheets structure formed in LiV_3O_8 . These LiV_3O_8 nanosheets are good candidates for cathode materials for high-energy lithium battery applications.

1. Introduction

Energy storage and conversion have unquestionably become top priorities in the 21st century because of the rapid depletion of fossil fuels and ecological concerns related to the combustion of fossil fuels (*e.g.*, air pollution, global warming, *etc.*). More environmentally benign and sustainable energy-storage systems are desired for future power sources.^{1–6} Lithium-ion batteries are considered to be the most promising energy-storage systems for consumer electronics, hybrid electrical vehicles, and electrical vehicles (EV) because of their high power output, long cycle life, and high energy density.^{7–11} However, to accelerate large scale commercialization of EVs, significant improvements are needed to reduce the cost and improve the safety and electrochemical features of these batteries.

One direction to explore are new cathode materials with high specific capacities.^{3,7} Vanadium-based cathode materials, such as V_2O_5 ,^{4,12} LiV_3O_8 ,¹³ VO_2 ,¹⁴ and their derivatives,^{15,16} have attracted significant attention because they can incorporate more than one lithium ion per vanadium atom, thus achieving higher specific capacities. For example, a specific discharge capacity of 442 mAh g⁻¹ can be obtained when three lithium ions intercalate into V_2O_5 , which is much higher than the capacity of 140 mAh g⁻¹ for LiCoO_2 . Lithium trivanadate (LiV_3O_8) is another vanadium oxide that also can incorporate several

lithium ions per formula.^{13,18,19} In addition, the structure reversibility of LiV_3O_8 is much better than that of V_2O_5 , so it has good potential to obtain stable capacity during long cycling. The monoclinic structure of $\text{Li}_{1+x}\text{V}_3\text{O}_8$, first reported by Wadsley in 1957,²⁰ consists of $(\text{V}_3\text{O}_8)^-$ layers oriented along a axis, connected by lithium ions at the octahedral sites in the interlayer. The excess lithium corresponding to the amount of x involved in the charge/discharge process is accommodated at the tetrahedral sites in the interlayer.²¹ Lithium ions residing in octahedral sites before lithium insertion act as a ‘pin’ for the layers and do not hinder the incoming lithium ions from occupying empty tetrahedral sites. This structure allows $\text{Li}_{1+x}\text{V}_3\text{O}_8$ to be restored to its original structure after the discharge/charge process.

However, in a practical cathode material, electrochemical properties, such as specific capacity, capacity retention, and rate capability, are strongly dependent on the particle morphology formed under different synthesis methods. A high-temperature, solid-state method described in the literature²² has been used extensively to prepare $\text{Li}_{1+x}\text{V}_3\text{O}_8$ electrodes. Because high-temperature treatment (*i.e.*, >600 °C, 10 h) usually leads to particle agglomeration and sintering, several other methods have been developed to synthesize LiV_3O_8 . These methods include a sol-gel process,^{23–25} a hydrothermal process,^{26,27} freeze-drying,^{28,29} spray drying,^{30,31} rheological phase reaction,³² ultrasonic preparation,^{33,34} flame pyrolysis,³⁵ low-heating solid-state reaction,³⁶ microwave or EDTA sol-gel preparation,^{37–39} and surfactant-assisted polymer precursor routes.²¹ In general, nanostructured materials such as nanorod structures,^{13,17,40,41} exhibit higher specific discharge capacities (>300 mAh g⁻¹) because of their reduced particle size and increased surface area. However, the capacity retentions of these materials (~70 percent) need to be further improved. For example, a sample synthesized by flame pyrolysis has a specific discharge capacity of

^aDepartment of Materials Science and Engineering, Central South University, Hunan, 410083, China. E-mail: sql@mail.csu.edu.cn

^bPacific Northwest National Laboratory, Richland, Washington, 99354, USA. E-mail: Jiguang.zhang@pnl.gov; jun.liu@pnl.gov

^cDepartment of Materials Science and Engineering, University of Washington, Seattle, WA, 98195, USA

† Electronic supplementary information (ESI) available: Fig. S1. See DOI: 10.1039/c1jm10976f

320 mAh g⁻¹ at the second cycle, but the discharge capacity decreases to 180 mAh g⁻¹ after 50 cycles.¹⁷ Micro-sized particles prepared by the surfactant-assisted polymer-precursor method²¹ and LiV₃O₈-polypyrrole (PPy) composite⁴² show relatively lower specific discharge capacities, but they possess better capacity retention (>90 percent). Therefore, a LiV₃O₈ material with both high discharge capacity and good capacity retention still needs to be developed.

In this work, we report, for the first time, a nanosheet-structured LiV₃O₈ electrode prepared by adding an appropriate polymer, as the structure-modifying agent, to the liquid precursor solutions during the synthesis process. The electrodes exhibit both excellent capacity and cycling stability. Various analytical methods, including X-ray diffraction (XRD), Raman spectroscopy, scanning electron microscopy (SEM), transmission electron microscopy (TEM), thermogravimetry (TG), and differential thermal analysis (DTA), were used to investigate the electrode compositions and structures, and the particle morphologies. The correlation between the excellent electrochemical performance and the microstructure of LiV₃O₈ are reported.

2. Experimental sections

All chemicals used in our study were analytical grade and were used as received without further purification. V₂O₅ (99.6%, Alfa Aesar), Li₂CO₃ (99+%, Sigma-Aldrich), and oxalic acid (H₂C₂O₄, 99+%, Sigma-Aldrich) were used to prepare the precursor solution. The oxalic acid was used as both a chelating and a reducing agent, and polyethylene glycol (PEG, 50% w/v, Optimize) was used as the structure modifier. First, V₂O₅ and oxalic acid in a stoichiometric ratio of 1 : 3 were dissolved in actively stirred de-ionized water at room temperature until a clear blue solution of VOC₂O₄ was formed. Then, a stoichiometric amount of Li₂CO₃ was added, and the mixture was vigorously stirred for 1 h. Next, 2 g of PEG with a molecular weight of 8000 was added drop by drop while stirring, and the resulting solution was heated overnight in an oven at 80 °C to produce the dry solid. The as-obtained material was calcined at 400 °C, 450 °C, 500 °C, and 550 °C in air for 2 h, and the samples obtained were designated LVO-400, LVO-450, LVO-500, and LVO-550, respectively. To investigate the thermal decomposition process, the same procedure was followed without adding PEG to the solution.

The crystalline structures of the prepared samples were determined by XRD using a Scintag XDS2000 θ - θ powder diffractometer equipped with a Ge (Li) solid-state detector and a Cu-K α sealed tube ($\lambda = 1.54178 \text{ \AA}$). The sample was scanned in a range between 10° to 70° (2 θ), with a step size of 0.02° and an exposure time of 10 s. Raman measurements were performed using an argon-ion laser with 514.5 nm wavelength excitation. A 20 mW laser was used for the Raman measurement, and no thermal effects were observed on the samples throughout the measurements. To control the exposure time, the laser beam was chopped using a mechanical shutter. Each Raman spectrum was obtained by accumulating 10 measurements, with exposure times of 20 s. A spectrometer (Princeton Instruments, Spectrapro 2500i) with a back illuminated charge-coupled detector attachment (Princeton Instruments, Spec 10) was used to obtain

Raman spectra. An SEM (FEI Helios 600 Nanolab FIB-SEM, 3 KV) was used to determine the particle morphology. The TEM analysis was carried out on a Jeol JEM 2010 microscope fitted with a LaB₆ filament and an acceleration voltage of 200 kV. A combined differential scanning calorimetry (DSC)/TGA instrument (Mettler-Toledo, TGA/DSC STAR system) was used to study the decomposition and reaction of the precursors.

The process used to prepare the cathode is described below. LiV₃O₈, Super P conductive carbon, and poly(vinylidene fluoride) (PVDF) binder in a weight ratio of 70 : 20 : 10 were mixed and then dispersed in a *N*-methylpyrrolidone (NMP) solution to make a slurry. LiV₃O₈, Super P conductive carbon, and poly(vinylidene fluoride) (PVDF) binder in a weight ratio of 70 : 20 : 10 were mixed and then dispersed in a *N*-methylpyrrolidone (NMP) solution to make a slurry. The ratio is chosen to have a direct comparison with previous published data on LiV₃O₈ nanoparticles such as those reported by Patey *et al.*³⁵ The slurry was coated on aluminum foil and dried in a vacuum oven at 100 °C overnight prior to coin-cell assembly. The Li/LiV₃O₈ cells (2325 type coin cells, National Research Council, Canada) were assembled in a glove box (Mbraun, Inc.) filled with ultra-high-purity argon using polypropylene membrane (3501, Celgard, Inc.) as the separator, Li metal as the anode, and 1-M LiPF₆ in ethyl carbonate/dimethyl carbonate (EC/DMC) (1 : 1 EC:DMC v/v) as the electrolyte. The charge/discharge performance of the electrodes were evaluated at room temperature using an Arbin Battery Tester BT-2000 (Arbin Instruments, College Station, Texas). The cyclic voltammetry (CV) curves were obtained using a CH Instruments Electrochemical Station (CH Instruments, Austin, Texas) in a voltage range of 1.5 to 4.0 V vs. Li/Li⁺.

3. Results and discussions

3.1 Structural characterization

The technique used to prepare the vanadyl oxalate precursor is similar to that described in our previous reports.^{4,13} The commercial V₂O₅ powder was added to the oxalic acid solution in a stoichiometric ratio of 1 : 3 while stirring until the color of the liquid changed from yellow to blue, which indicated that the valence had changed from V⁵⁺ to V⁴⁺ and that vanadyl oxalate hydrate (VOC₂O₄·*n*H₂O) had formed. This reaction can be expressed as shown below:



In the next step, a stoichiometric amount of Li₂CO₃ was added to the blue precursor solution. PEG then was added into the solution, and the precursor mixture was obtained after drying the liquid in air at 80 °C overnight. Fig. 1 shows the TG and DTA results of the LiV₃O₈ precursor (a) and precursor containing PEG (b) under flowing air with a temperature ramping rate of 5 °C/min. The slow weight-loss between 30 °C and 250 °C shown in Fig. 1a can be attributed to the loss of physically and chemically bonded water in the precursor. The significant weight loss shown on the TG curve and a corresponding exothermal peak on the DTA curve between 250 °C and 320 °C are related to the decomposition of inorganic precursors. Later, a small weight

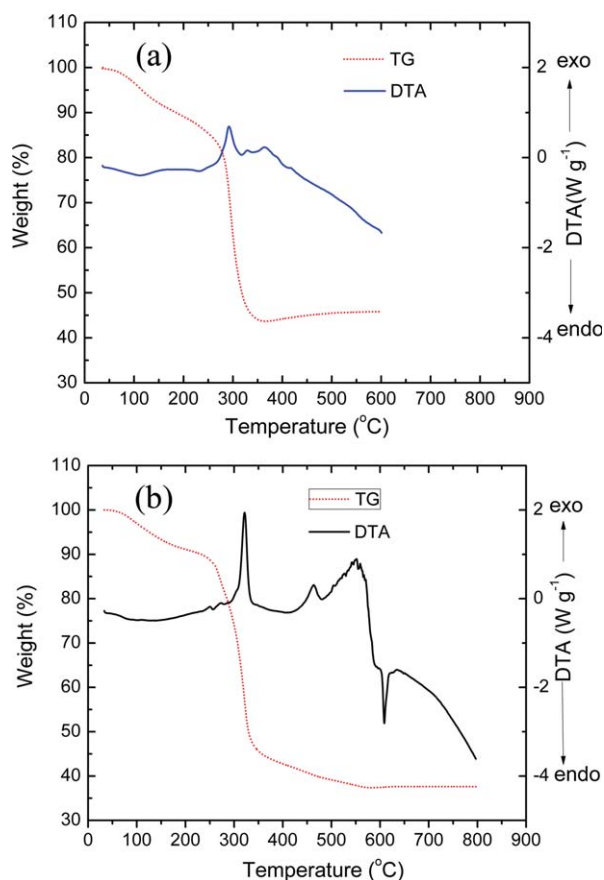


Fig. 1 TG and DTA data for the precursor (a) and the precursor with the addition of PEG (b).

increase and two small exothermal peaks are detected. The small exothermal peaks, which correspond to two heat-release reactions, probably resulted from the combustion of a small amount of residual carbon and the further oxidation of V^{4+} in air. The net increase in total weight suggests that the extra weight gained from oxidation of V^{4+} overwhelms the mass loss of carbon in this process. The brown color of the material after the TG experiment is typical of LiV_3O_8 .

Fig. 1b shows the TG and DTA results for the precursor with the addition of PEG. No significant difference was detected between the two TG curves between 30 °C and 250 °C, suggesting similar water-loss processes. The small difference could result from the existence of PEG, which might contain less water after drying at 80 °C. A rapid weight loss also was detected for the precursor with the addition of PEG between 250 °C and 320 °C. However, the exothermal peak intensity on the DTA curve (shown in Fig. 1b) is much higher than that without the addition of PEG in the precursor. The extra heat is generated from the decomposition of PEG within this temperature range. The smaller weight loss is attributed to the smaller weight change from PEG to its decomposition product (carbon) in this process, compared to the weight loss of the precursor (shown in Fig. 1a). The gradual weight loss that occurs between 320 °C and 600 °C results from carbon combustion in air. Although the percentage of and the degree of crystallinity of LiV_3O_8 in the composite increase between 320 °C and 600 °C, the weight loss of carbon

from combustion is greater than the weight increase from the oxidation process in which oxygen atoms are added. An endothermic peak on the DTA curve at 600 °C and a flat plateau on the TG curve indicate melting of the LiV_3O_8 and total oxidation of vanadium to V^{5+} .

Fig. 2 shows the XRD patterns (a) of the samples prepared at different temperatures (400 °C, 450 °C, 500 °C, and 550 °C) and the Raman results (b) for LVO-400 and LVO-500 samples. For the LVO-400 sample, several main peaks assigned to the monoclinic LiV_3O_8 are detected, indicating the initial formation of LiV_3O_8 in the weight-loss process at 400 °C. However, when compared samples prepared at higher temperatures, the degree of crystallinity is relatively smaller, and the peak positions are slightly left-shifted. As shown in Fig. 2b, the typical D band (around 1400 cm^{-1})⁴³ and G band (around 1650 cm^{-1})^{44,45} assigned to carbon are present, suggesting the existence of large amount of carbon. Only a small, broad bump around the G-band position is observed for the LVO-500 sample, which demonstrates the significant decrease of residual carbon in the material. This result agrees well with the black color of the LVO-400 sample and the small weight loss that occurs between 320 °C and 600 °C. The peaks at 777 cm^{-1} , 966 cm^{-1} , and 1099 cm^{-1} are consistent with the typical Raman patterns of LiV_3O_8 .^{38,46} The peak occurring at 777 cm^{-1} probably is due to the corner-sharing oxygen atomic motions. The two high-frequency bands at 966 cm^{-1} and 1099 cm^{-1} are attributed to the vibrational modes belonging to the A_g symmetry, and can be assigned to V–O stretching vibrations of VO_5 pyramids.³⁸ Higher peak intensities and more peaks in the XRD pattern are observed for samples synthesized at higher temperatures. As shown by the Raman spectroscopy results, the peak intensities occurring at 777 cm^{-1} , 966 cm^{-1} , and 1099 cm^{-1} also increase. The XRD patterns can be assigned to the known layered-type LiV_3O_8 (JCPDS 72-1193) with a monoclinic crystalline structure of the $P21/m$ space group. Although the black color is observed for all the samples, the color becomes quite different after grinding in a mortar. The LVO-400 and LVO-450 samples were black or grey after grinding, while the LVO-500 and LVO-550 samples were the typical brown color. Figure S1 (see ESI)† shows the color of LVO-500 material before (a) and after grinding in a mortar. The LVO-500 sample obtained by calcinations in air at 500 °C for 2 h exhibits black color. But after grinding by hand in a mortar, the color is changed to the typical brown color of LiV_3O_8 . In the whole process, no other material was added and only mechanical grinding was employed. So no phase change should happen.

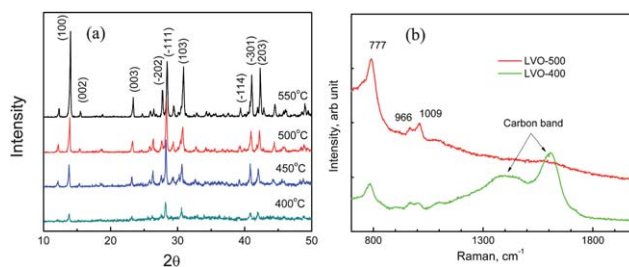


Fig. 2 XRD patterns (a) for the samples fabricated at different temperatures and (b) Raman results for the LVO-400 and LVO-500 samples.

According to the Raman results for LVO-500 material, the G band is very weak, which indicates the small amount of carbon in the final products after calcinations. The black color was assigned to the residual carbon from the decomposition of PEG. It covers the surface of LiV_3O_8 material with a black color. However, after grinding, the agglomerates were broken up and the carbon did not cover all the surface of the particles, so that the typical color of LiV_3O_8 was displayed. However, LVO-400 sample still shows the black color even after grinding because of the large amount of carbon in the LVO-400. This is evidenced by the obvious G and D band by the Raman results.

The unique nanosheet structure and morphology of the as-prepared LVO-500 sample was revealed by SEM and TEM studies, as shown in Fig. 3. In Fig. 3a, white arrows at the top and the bottom of the particles point to the layered sheets. A higher magnification SEM image (shown in Fig. 3b) gives a clearer picture of the layered structure. The top thick layer actually is composed of three thinner layers. The image reveals ample space between the top thick sheets and the lower sheets. It is interesting that the layer-by-layer stacking structure is coherent in the whole image, and the thin layers also are well separated.

The nanosheet structure is further confirmed by the TEM images (shown in Fig. 3c and 3d) of LVO-500. These images show the face-on layer structure on top of one another. As indicated by numbers in Fig. 3c and 3d, at least three layers can be identified. The dark area (numbered '1') contains three layers, the bright area ('3') contains one layer, and the grey area ('2') contains two layers. This result is in good agreement with the SEM study, which revealed the layer-by-layer stacking structures. This structure is quite unique in LiV_3O_8 and is different from the nanorod-structured LiV_3O_8 described in our recent publication.¹³ The structural change indicates that PEG has played a key role in nanosheet-structure formation. The space between each layer probably results from the decomposition of

PEG and the loss of residual carbon during the oxidation process in air. The study of the mechanism of nanosheet formation is under the way and will be reported later.

3.2 Electrochemical performance

Fig. 4 shows the electrochemical properties of samples synthesized at 400 °C, 450 °C, 500 °C, and 550 °C. Fig. 4a shows the second-cycle discharge/charge curves of the four samples in the voltage range between 1.5 V and 4.0 V vs. Li/Li^+ at 100 mA g^{-1} . The LVO-400 sample only shows small characteristic plateaus for LiV_3O_8 . However, the discharge/charge curves of LVO-450, LVO-500, and LVO-550 are consistent with typical lithium-ion intercalation and de-intercalation in/from LiV_3O_8 crystalline structures reported in the literature.^{13,27} The specific discharge capacities rank in the following order: LVO-500 > LVO-550 > LVO-450 > LVO-400. Fig. 4b shows the cycling performances of the four samples from the first cycle to the one-hundredth cycle. Initial specific discharge capacity increases from the first to the second cycles were observed for all the samples. These increases can be mainly attributed to the extraction of lithium ions in LiV_3O_8 at high voltage (*i.e.*, 3.7 V) during the first charge process. This is evidenced by the larger specific charge capacities than their corresponding specific discharge capacities at the 1st cycle. For instance, the first specific charge capacity of LVO-500 electrode is 260 mAh g^{-1} , which is larger than the 1st specific discharge capacity of 240 mAh g^{-1} . The removal of small amount of pre-existence Lithium from LiV_3O_8 can provide more empty sites for the 2nd cycle's lithium insertion. Furthermore, the improved wettability of the electrodes after the first cycle may also contribute to the capacity increase.

Fig. 4b compares the cycle stabilities of the four electrodes by showing their specific discharge capacities *versus* cycles. It is worth noting that the LVO-500 and LVO-550 electrodes have both better cycle stabilities and higher specific discharge capacities than the two electrodes synthesized at lower temperatures (LVO-400 and LVO-450). The open-circuit potentials of LVO-400 and LVO-450 are 3.0 V and 3.2 V vs. Li/Li^+ , respectively, which are much lower than the 3.59 V and 3.60 V potentials for the LVO-500 and LVO-550 electrodes. The lower open-circuit potentials can be attributed to the impurity for the lower-temperature fabricated electrodes. As evidenced by the thermogravimetric and Raman results, more carbon remaining in the final materials for LVO-400 suggesting it is more difficult to fully oxidize V to V^{5+} in the materials. In other words, the impurity of vanadium oxide synthesized at lower-temperature is high. This kind of impurity would decrease the open circuit potential of the electrodes. The poorer stabilities for the LVO-400 and LVO-450 electrodes are attributed to the higher impurity content and the lower crystallinity of LiV_3O_8 electrodes. The impurity of vanadium oxides would cause electrolyte decomposition, and these materials may not participate in the reaction during the charge/discharge process, thus reducing the reversibility of the whole electrode in the cycling tests. Furthermore, the lower crystallinity indicates a higher disorder of atoms within the LiV_3O_8 lattice structure. The higher disorder may block the diffusion path of the lithium ions within the LiV_3O_8 host material and degrade its reversibility and cycle stability. This phenomenon also has been extensively studied in lithium metal oxides, such as LiNiO_2 .⁴⁷⁻⁴⁹

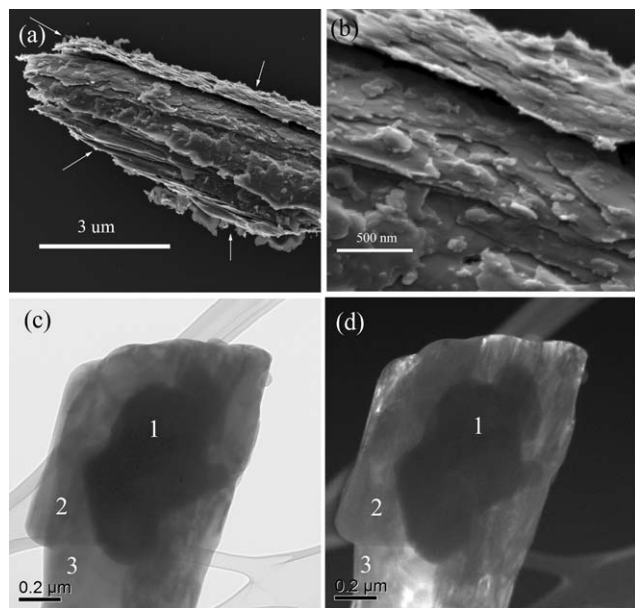


Fig. 3 SEM images of the LVO-500 sample at low (a) and high (b) magnification and its TEM images taken at a bright field (c) and a dark field (d).

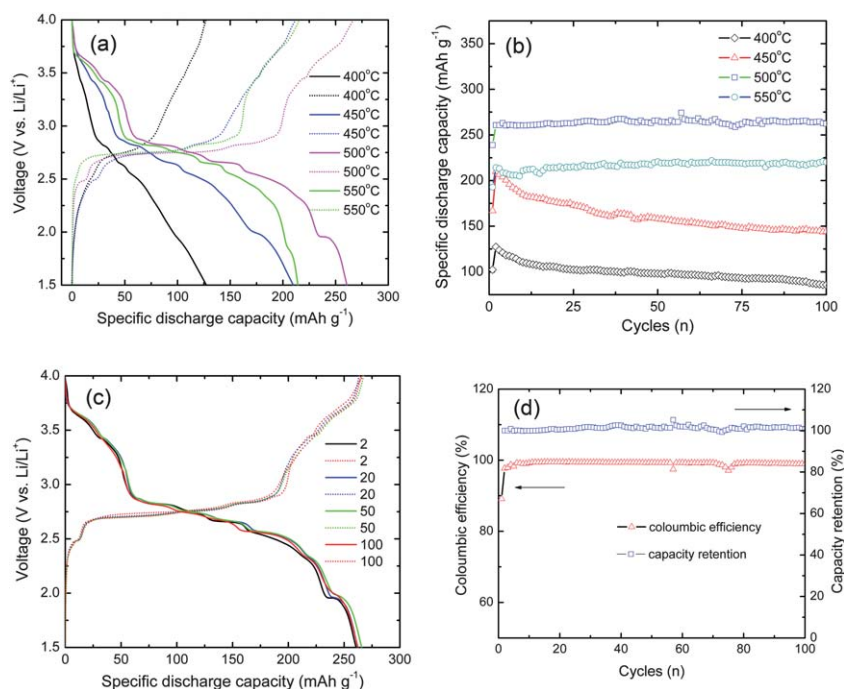


Fig. 4 (a) Second-cycle discharge/charge curves, (b) the cycling performances of samples fabricated at different temperatures (400 °C, 450 °C, 500 °C, and 550 °C) at 100 mA g⁻¹, (c) discharge/charge curves at different cycles, and (d) coulombic efficiencies and capacity retention plots of the LVO-500 electrode.

We observed excellent cycle stabilities for the LVO-500 and LVO-550 electrodes. However, the specific discharge capacity of the LVO-500 sample is much higher than that of LVO-550 sample, probably because of the different kinetics for lithium ions diffusion in the electrode. As there is not much carbon left in the LVO-500 sample, further increasing the calcination temperature could cause the LiV₃O₈ particles to grow larger, thus hindering the transport of lithium ions. Fig. 4c shows the discharge/charge curves at the second, twentieth, thirtieth, fiftieth, and one-hundredth cycles for the LVO-500 electrode. The specific discharge capacities are 260.7 mA h g⁻¹, 262.2 mA h g⁻¹, 265.7 mA h g⁻¹, and 262.4 mA h g⁻¹ at the second, twentieth, thirtieth, fiftieth, and one-hundredth cycles, respectively. The corresponding specific charge capacities are 266.8 mA h g⁻¹, 263.5, 267.5 mA h g⁻¹, and 265.1 mA h g⁻¹ and the coulombic efficiencies are 97.7 percent, 99.4 percent, 99.3 percent, and 99 percent. No capacity fading is observed between second and one-hundredth cycles, and the specific discharge capacities and the discharge/charge curves for these cycles are about the same. Fig. 4d shows the coulombic efficiencies and capacity retentions of the LVO-500 electrode between first and one-hundredth cycles. Capacity retention is based on the specific discharge capacity of the second cycle. Very good capacity retentions and high coulombic efficiencies are observed from the second to the one-hundredth cycles.

The superior electrochemical performances of the materials described in this paper are attributed to the unique layer-by-layer stacked nanosheet structures. As shown in Fig. 3, the ample space between each sheet would allow easy penetration of electrolyte, thus increasing the interfacial area between the electrode and the electrolyte. In addition, the thickness of the nanosheets is

less than 50 nm, which would decrease the lithium-ion diffusion and the electron transportation distance. Furthermore, the nanosheet structure may be more capable of maintaining the integrity of the structure than other LiV₃O₈ electrode materials. Because several lithium ions intercalate into the active materials, lattice expansion can potentially breakdown the crystalline structure, resulting in capacity fading over many cycles. Thin, layer-by-layer structured nanosheets tolerate structural variations during the charge/discharge process, leading to a better cyclic stability.

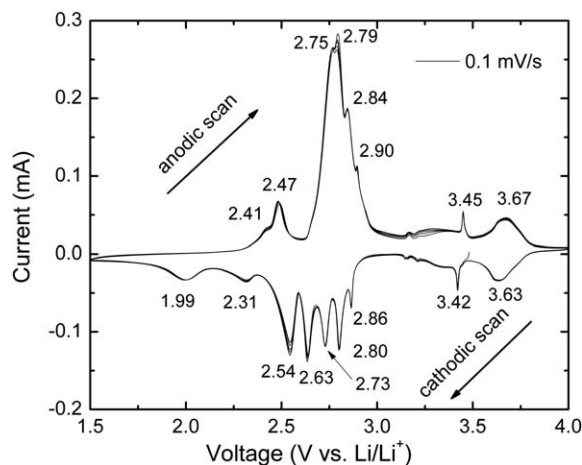


Fig. 5 CV curves of five cycles of LVO-500 electrode at a scan rate of 0.1 mV s⁻¹ between 1.5 V and 4.0 V.

Fig. 5 shows five CV curves of the LVO-500 electrode at 0.1 mV s^{-1} . The peaks corresponding to the lithium intercalation/de-intercalation are well preserved. During the cathodic scan, nine obvious peaks at 3.63 V, 3.42 V, 2.86 V, 2.80 V, 2.73 V, 2.63 V, 2.54 V, 2.31 V, 1.99 V vs. Li/Li^+ are clearly observed. These peaks demonstrate the multiple phase transitions that occur during the lithium-ion intercalation process. In the anodic scan, eight peaks at 2.41 V, 2.47 V, 2.75 V, 2.79 V, 2.84 V, 2.90 V, 3.45 V, and 3.67 V vs. Li/Li^+ were observed. The well-observed peaks in our experiment are largely attributed to the novel nanosheet-structures. As shown in Fig. 3, the space between nanosheets is clearly observed, which facilitates the electrolyte penetration and reduce the energy barrier for Li^+ ion intercalation/de-intercalation. Therefore the phase change can happen rapidly. The five CV curves shown in Fig. 5 are almost superimposed over each other, except for a very small difference observed at 2.79 V and 2.54 V. The peak positions shown on the CV curves correspond well with the discharge/charge plateaus (shown in Fig. 4c). The anodic scan peak observed at 3.67 V results from extraction of pre-existence lithium in LiV_3O_8 starting materials, which allows intercalation of more lithium ions during the next cycle, in turn, explains the capacity increase observed from the first cycle to the second cycle. The good agreement of the five CV curves demonstrates good structural reversibility and good cycle stability for the LVO-500 electrode.

Fig. 6 shows the Nyquist plot of LiV_3O_8 with different structures at 3.5 V vs. Li/Li^+ . The micro-sized particle was synthesized using the conventional high-temperature (680°C , 10 h) method.¹³ The Nyquist plot of the nanosheet-structured LiV_3O_8 electrode reported in this work also is presented. Because the electrode and electrolyte fabrication processes are the same, differences between the resistances should be related to the electrode materials. A resistance of 60Ω was detected for nanosheet-structured electrode, which is much less than 200Ω resistance measured for the micro-sized electrode. These lower resistances indicate that charge transfer is easier in nanosheets electrodes. The ample spaces between the layers facilitate electrolyte penetration and increase the interfacial contact area between electrolyte and electrode. Because of the reduced electron transportation distance in nanoscale materials, electrons

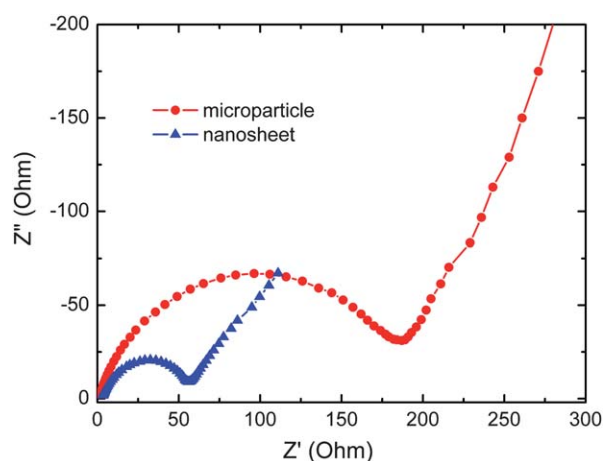


Fig. 6 Nyquist plot of LiV_3O_8 of different structures at 3.5 V vs. Li/Li^+ .

can be effectively transferred. Furthermore, the small amount of residual carbon present, as indicated by the black color of the material, also contributes to faster charge transfer rates.

Fig. 7 shows the cycling performances of the LVO-500 electrode at different current densities. As shown in Fig. 6, the LVO-500 electrode exhibits very good cycle stability between the second and one-hundredth cycles at three different current densities. The specific discharge capacities at second cycle are of 260 mAh g^{-1} , 194 mAh g^{-1} , and 166 mAh g^{-1} at current densities of 100 mA g^{-1} , 300 mA g^{-1} , and 1000 mA g^{-1} , respectively. After 100 cycles, specific discharge capacities of 262 mAh g^{-1} , 181 mAh g^{-1} , and 157 mAh g^{-1} can be retained. The results demonstrate very good capacity retention.

Table 1 compares previous results reported on LiV_3O_8 synthesis and their electrochemical properties with the results of our study. As can be seen, the nanosheets exhibit almost the highest initial capacity, and also the best stability without any capacity fading. Only a few other studies reported a slightly higher initial capacity—that is, the sol-gel method,³⁶ Ag doping,⁴¹ and our previously reported soft-chemistry method.¹³ Materials produced using the sol-gel method have an initial specific discharge capacity of 281 mAh g^{-1} , but the capacity decreases to 200 mAh g^{-1} at even lower current density of 40 mA g^{-1} with 71 percent capacity retention. Although Ag-doped LiV_3O_8 electrodes⁴¹ have a higher capacity of 328 mAh g^{-1} at a current density of 150 mA g^{-1} , the capacity decreases rapidly to 252.7 mAh g^{-1} after 50 cycles, and the capacity retention only is about 77 percent. Recently, a nanorod structured LiV_3O_8 electrode prepared using the soft-chemistry method¹³ obtained a maximum specific discharge capacity of 320 mAh g^{-1} . This material retained a discharge capacity of 250 mAh g^{-1} over 100 cycles with a current density of 100 mA g^{-1} . Significant capacity fading during the initial cycles was observed, and the capacity retention needs to be improved further. LiV_3O_8 electrodes with good capacity retention have been fabricated by the solution route (99 percent),⁴² spray drying (84 percent),³¹ the polymer method (99 percent),²¹ and the hydrothermal method (96 percent)²⁷ have been reported, but the specific capacities of

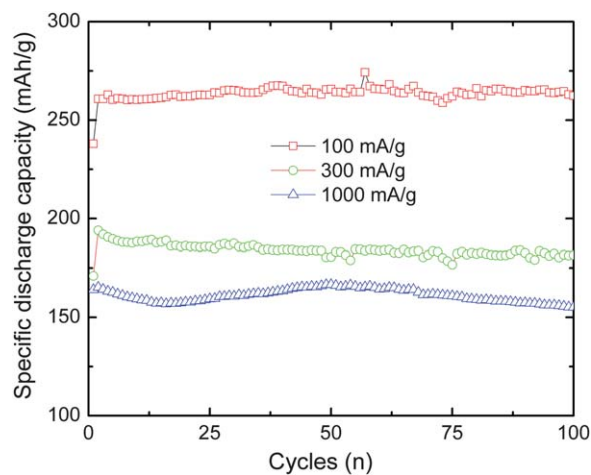


Fig. 7 Cycling performance of the LVO-500 electrode at different current densities (100 mA g^{-1} , 300 mA g^{-1} , and 1000 mA g^{-1}) between 1.5 V and 4.0 V vs. Li/Li^+ .

Table 1 Comparison on electrochemical properties of LiV_3O_8 prepared by different methods²¹

Synthesis Method ^(ref)	Composition	Current Density (mA g ⁻¹)	Capacity (mAh/g) (cycle number)	Capacity Retention (%)
Hydrothermal ⁵⁰	LiV_3O_8	120	212.8 (1)–152.1 (18)	72
Sol-gel ³⁶	$\text{Li}_{1.2}\text{V}_3\text{O}_8$	60	281 (2)–200 (40)	71
Sol-gel ⁴¹	$\text{Li}_{0.96}\text{Ag}_{0.04}\text{V}_3\text{O}_8$	150	328 (1)–252.7 (50)	77
Flame pyrolysis ¹⁷	LiV_3O_8	100	271 (1)–180 (50)	66
Solution route ⁴²	LiV_3O_8 -polypyrrole (PPy) composite	40	184 (1)–183 (100)	99
Spray drying ³¹	$\text{Li}_{1.1}\text{V}_3\text{O}_8$	116	260 (2)–220 (60)	84
Hydrothermal ²⁷	LiV_3O_8	100	Stabilized at 236 (100)	96
Polymer method ²¹	LiV_3O_8	120	182 (2)–180 (60)	99
Soft chemistry ¹³	LiV_3O_8	100	320 (2)–250 (100)	78
Present work	LiV_3O_8	100	260 (2)–262 (100)	100

these materials are much lower (about 180 mAh g⁻¹). For example, the LiV_3O_8 -polypyrrole composite electrode produced using the solution route only has a specific capacity of 183 mAh g⁻¹, the value of which is quite similar to the specific capacity of a LiV_3O_8 electrode synthesized using the polymer method. When compared to the materials described in these earlier reports, the LiV_3O_8 nanosheets reported in this paper not only exhibit excellent capacity retention (100 percent), but also show a relatively high specific discharge capacity of 260 mAh g⁻¹ at a current density of 100 mA g⁻¹. It also exhibits the highest specific discharge capacity after 100 cycles. An energy density of 705 kWh kg⁻¹ can be obtained at 100 mA g⁻¹, the energy density of which is much higher than that of LiCoO_2 and LiFePO_4 electrodes. Furthermore, the fabrication method described in this paper does not require special equipment, and can be easily scaled up for large quantity production. Therefore, the LiV_3O_8 nanosheet prepared by our new method is a promising cathode material for high-capacity, long-cycle life-applications. This method also can be used in other electrode-material synthesis techniques to improve their performance of the resulting materials.

4. Conclusions

Nanosheet-structured LiV_3O_8 cathode materials were successfully synthesized by adding PEG polymer as a structure modifier during the LiV_3O_8 synthesis process. The effect of calcination temperature on the electrochemical performance of LiV_3O_8 was investigated. Samples calcined at 500 °C demonstrated the best performance—that is, an initial specific discharge capacity of 260 mAh g⁻¹ and excellent capacity retention (100 percent) at 100 mA g⁻¹. After 100 cycles, a specific discharge capacity of 262 mAh g⁻¹ was retained, which is among the best performances ever reported. This excellent electrochemical performance is attributed to the following characteristics of the novel nanosheet-structure: 1) the ample space between each layer allows easier penetration of the electrolyte, 2) the nanoscale thickness of the nanosheet facilitates fast diffusion of lithium ions, and 3) the nanosheet-structure can tolerate larger structural variations than nanorod-structures.

Acknowledgements

We acknowledge the financial support provided by the National Nature Science Foundation of China (No. 50774097), the

Creative Research Group of the National Natural Science Foundation of China (No. 50721003), the Laboratory Directed Research and Development Program of Pacific Northwest National Laboratory (PNNL), and the Batteries for the Advanced Transportation Technologies program of Office of Vehicle Technology of the U.S. Department of Energy (DOE). A. Pan appreciates the financial support from the Chinese Council Scholarship. The TEM work was performed at the Environmental Molecular Sciences Laboratory, a national scientific-user facility sponsored by the DOE Office of Biological and Environmental Research. The DOE Office of Basic Energy Sciences, Division of Materials Sciences and Engineering, also provided support under Award KC020105-FWP12152. PNNL is operated for DOE by Battelle Memorial Institute.

References

- 1 M. Winter and R. J. Brodd, What are Batteries, Fuel cells, and Supercapacitors?, *Chem. Rev.*, 2004, **104**, 4245–4269.
- 2 M. S. Whittingham, Lithium Batteries and Cathode Materials, *Chem. Rev.*, 2004, **104**, 4271–4301.
- 3 D. Liu and G. Cao, Engineering Nanostructured Electrodes and Fabrication of Film Electrodes for Efficient Lithium Ion Intercalation, *Energy Environ. Sci.*, 2010, **3**, 1218–1237.
- 4 A. Pan, J.-G. Zhang, Z. Nie, G. Cao, B. W. Arey, G. Li, S. Liang and J. Liu, Facile Synthesized Nanorod Structured Vanadium Pentoxide for High-Rate Lithium Batteries, *J. Mater. Chem.*, 2010, **20**, 9193–9199.
- 5 A. Pan, J. Liu, J.-G. Zhang, W. Xu, G. Cao, Z. Nie, B. W. Arey and S. Liang, Nano-Structured $\text{Li}_3\text{V}_2(\text{PO}_4)_3/\text{Carbon}$ Composite for High-Rate Lithium-Ion Batteries, *Electrochem. Commun.*, 2010, **12**, 1674–1677.
- 6 A. Pan, D. Choi, J.-G. Zhang, S. Liang, G. Cao, Z. Nie, B. W. Arey and J. Liu, High-Rate Cathodes Based on $\text{Li}_3\text{V}_2(\text{PO}_4)_3$ Nanobelts Prepared via Surfactant-Assisted Fabrication, *J. Power Sources*, 2011, **196**, 3646–3649.
- 7 J.-M. Tarascon and M. Armand, Issues and Challenges Facing Rechargeable Lithium Batteries., *Nature*, 2001, **414**, 359–367.
- 8 Y. Wang and G. Cao, New Developments of Nanostructured Cathode Materials for Highly Efficient Lithium Ion Batteries, *Adv. Mater.*, 2008, **20**, 2251–2269.
- 9 S. F. Yang, P. Y. Zavalij and M. S. Whittingham, Hydrothermal Synthesis of Lithium Iron Phosphate Cathodes, *Electrochem. Commun.*, 2001, **3**, 505–508.
- 10 A. Pan, D. Liu, X. Zhou, B. B. Garcia, S. Liang, J. Liu and G. Cao, Enhanced Lithium-ion Intercalation Properties of Coherent Hydrated Vanadium pentoxide-Carbon Cryogel Nanocomposites, *J. Power Sources*, 2010, **195**, 3893–3899.
- 11 B. L. Ellis, K. T. Lee and L. F. Nazar, Positive Electrode Materials for Li-ion and Li-Batteries, *Chem. Mater.*, 2010, **22**, 691–714.
- 12 L. Q. Mai, L. Xu, C. H. Han, Y. Z. Luo, S. Y. Zhao and Y. L. Zhao, Electrospun Ultralong Hierarchical Vanadium Oxide Nanowires with

- High Performance for Lithium Ion Batteries, *Nano Lett.*, 2010, **10**, 4750–4755.
- 13 A. Pan, J. Liu, J.-G. Zhang, G. Cao, W. Xu, Z. Nie, X. Jie, D. Choi, B. W. Arey, C. Wang and S. Liang, Template Free Synthesis of LiV_3O_8 Nanorods as a Cathode Material for High-Rate Secondary Lithium Batteries, *J. Mater. Chem.*, 2011, **21**, 1153–1161.
 - 14 H. Liu, Y. Wang, K. Wang, E. Hosono and H. Zhou, Design and Synthesis of a Novel Nanothorn VO_2 (B) Hollow Microsphere and Their Application in Lithium Ion Batteries, *J. Mater. Chem.*, 2009, **19**, 2835–2840.
 - 15 N. A. Chernova, M. Roppolo, A. C. Dillion and M. S. Whittingham, Layered Vanadium and Molybdenum Oxides: Batteries and Electrochromics, *J. Mater. Chem.*, 2009, **19**, 2526–2552.
 - 16 M. S. Whittingham, Y. Song, S. Lutta, P. Y. Zavalij and N. A. Chernova, Some Transition Metal (Oxy)phosphates and Vanadium Oxides for Lithium Batteries, *J. Mater. Chem.*, 2005, **15**, 3362–3379.
 - 17 S.-H. Ng, T. J. Patey, R. Buchel, F. Krumeich, J.-Z. Wang, H. Liu, S. E. Pratsinis and P. Novak, Flame Spray-pyrolyzed Vanadium Oxide Nanoparticles for Lithium Battery Cathodes, *Phys. Chem. Chem. Phys.*, 2009, **11**, 3748–3755.
 - 18 Q. Shi, R. Z. Hu, L. Z. Ouyang, M. Q. Zeng and M. Zhu, High-Capacity LiV_3O_8 Thin-Film Cathode with a Mixed Amorphous-Nanocrystalline Microstructure Prepared by RF Magnetron Sputtering, *Electrochem. Commun.*, 2009, **11**, 2169–2172.
 - 19 Y. Feng, F. Hou and Y. Li, A New Low-temperature Synthesis and Electrochemical Properties of LiV_3O_8 Hydrate as Cathode Material for Lithium-Ion Batteries, *J. Power Sources*, 2009, **192**, 708–713.
 - 20 A. D. Wadsley, Crystal Chemistry of Non-stoichiometric Pentavalent Vanadium Oxides: Crystal Structure of $\text{Li}_{1+x}\text{V}_3\text{O}_8$, *Acta Crystallogr.*, 1957, **10**, 261–267.
 - 21 A. Sakunthala, M. V. Reddy, S. Selvasekarapandian, B. V. R. Chowdari and P. C. Selvin, Preparation, Characterization, and Electrochemical Performance of Lithium Trivanadate Rods by a Surfactant-Assisted Polymer Precursor Method for Lithium Batteries, *J. Phys. Chem. C*, 2010, **114**, 8099–8107.
 - 22 G. Pistoia, S. Panero, M. Tocci, R. V. Moshkev and V. Manev, Solid Solutions $\text{Li}_{1+x}\text{V}_3\text{O}_8$ as Cathodes for High Rate Secondary Li Batteries, *Solid State Ionics*, 1984, **13**, 311–318.
 - 23 K. P. Lee, K. M. Manesh, K. S. Kim and A. Y. Gopalan, Synthesis and Characterization of Nanostructured Wires (1D) to Plates (3D) LiV_3O_8 Combining Sol-Gel and Electrospinning Processes, *J. Nanosci. Nanotechnol.*, 2009, **9**, 417–422.
 - 24 Y. X. Gu and F. F. Jian, Facile Preparation and Electrochemical Properties of Large-scale $\text{Li}_{1+x}\text{V}_3\text{O}_8$ Nanobelts, *J. Sol-Gel Sci. Technol.*, 2008, **46**, 161–165.
 - 25 L. Liu, L. F. Jiao, Y. H. Zhang, J. L. Sun, L. Yang, Y. L. Miao, H. T. Yuan and Y. M. Wang, Synthesis of LiV_3O_8 by an Improved Citric Acid Assisted Sol-gel Method at Low Temperature, *Mater. Chem. Phys.*, 2008, **111**, 565–569.
 - 26 X. Li, P. Li, M. Luo, X. Chen and J. Chen, Controllable Solvo-hydrothermal Electrodeposition of Lithium Vanadate Uniform Carnate-Like Nanostructure and Their Electrochemical Performance, *J. Solid State Electrochem.*, 2010, **14**, 1325–1332.
 - 27 H. Liu, Y. Wang, K. X. Wang, Y. R. Wang and H. S. Zhou, Synthesis and Electrochemical Properties of Single-Crystalline LiV_3O_8 Nanorods as Cathode Materials for Rechargeable Lithium Batteries, *J. Power Sources*, 2009, **192**, 668–673.
 - 28 K. West, B. Zachaerchristiansen, S. Skaarup, Y. Saidi, J. Barker, I. I. Olsen, R. Pynenburg and R. Loksang, Comparison of LiV_3O_8 Cathode Materials Prepared by Different Methods, *J. Electrochem. Soc.*, 1996, **143**, 820–825.
 - 29 O. A. Brylev, O. A. Shlyakhtin, A. V. Egorov and Y. D. Tretyakov, Phase Formation and Electrochemical Properties of Cryochemically Processed $\text{Li}_{1+x}\text{V}_3\text{O}_8$ Materials, *J. Power Sources*, 2007, **164**, 868–873.
 - 30 M. Y. Saidi, I. Olsen, R. Koksang, J. Barker, R. Pynenburg, K. West, B. Zachaerchristiansen, S. Skaarup, in *Solid State Ionics IV*, Schreiber M., Nazri and Tarascon, ed., 1995, pp 201–209.
 - 31 N. Tran, K. G. Bramnik, H. Hibst, J. Prolss, N. Mronga, M. Holzapfel, W. Scheifele and P. Novak, Spray-drying Synthesis and Electrochemical Performance of Lithium Vanadates as Positive Electrode Materials for Lithium Batteries, *J. Electrochem. Soc.*, 2008, **155**, A384–A389.
 - 32 Q. Y. Liu, H. W. Liu, X. W. Zhou, C. J. Cong and K. L. Zhang, A Soft Chemistry Synthesis and Electrochemical Properties of LiV_3O_8 as Cathode Material for Lithium Secondary Batteries, *Solid State Ionics*, 2005, **176**, 1549–1554.
 - 33 N. Kumagai and A. S. Yu, Ultrasonically Treated LiV_3O_8 as a Cathode Material for Secondary Lithium Batteries, *J. Electrochem. Soc.*, 1997, **144**, 830–837.
 - 34 Y. M. Liu, X. C. Zhou and Y. L. Guo, Effects of Reactant Dispersion on the Structure and Electrochemical Performance of $\text{Li}_{1.2}\text{V}_3\text{O}_8$, *J. Power Sources*, 2008, **184**, 303–307.
 - 35 T. J. Patey, S. H. Ng, R. Buchel, N. Tran, F. Krumeich, J. Wang, H. K. Liu and P. Novak, Electrochemistry of LiV_3O_8 Nanoparticles Made by Flame Spray Pyrolysis, *Electrochem. Solid-State Lett.*, 2008, **4**, A46–A50.
 - 36 J. G. Xie, J. X. Li, H. Zhan and Y. H. Zhou, Low-temperature Sol-gel Synthesis of $\text{Li}_{1.2}\text{V}_3\text{O}_8$ from V_2O_5 Gel, *Mater. Lett.*, 2003, **57**, 2682–2687.
 - 37 F. Wu, L. Wang, C. Wu, Y. Bai and F. Wang, Study on $\text{Li}_{1+x}\text{V}_3\text{O}_8$ Synthesized by Microwave Sol-gel Route, *Mater. Chem. Phys.*, 2009, **115**, 707–711.
 - 38 G. Yang, G. Wang and W. H. Hou, Microwave Solid-State Synthesis of LiV_3O_8 as Cathode Material for Lithium Batteries, *J. Phys. Chem. B*, 2005, **109**, 11186–11196.
 - 39 Y. Zhou, H. F. Yue, X. Y. Zhang and X. Y. Deng, Preparation and Characterization of LiV_3O_8 Cathode Material for Lithium Secondary Batteries through an EDTA-Sol-Gel Method, *Solid State Ionics*, 2008, **179**, 1763–1767.
 - 40 S. Jouanneau, A. L. G. L. Salle, A. Verbaere, M. Deschamps, S. Lascaud and D. Guyomard, Influence of The Morphology on The Li Insertion Properties of $\text{Li}_{1.1}\text{V}_3\text{O}_8$, *J. Mater. Chem.*, 2003, **13**, 921–927.
 - 41 J. Sun, L. Jiao, H. Yuan, L. Liu, X. Wei, Y. Miao, L. Yang and Y. Wang, Preparation and Electrochemical Performance of $\text{Ag}_x\text{Li}_{1-x}\text{V}_3\text{O}_8$, *J. Alloys Compd.*, 2009, **472**, 363–366.
 - 42 S. Y. Chew, C. Feng, S. H. Ng, J. Wang, Z. Guo and H. Liu, Low-Temperature Synthesis of Polypyrrole-Coated LiV_3O_8 Composite with Enhanced Electrochemical Properties, *J. Electrochem. Soc.*, 2007, **154**, A633–A637.
 - 43 M. S. Dresselhaus, G. Dresselhaus, R. Saito and A. Jorio, Raman Spectroscopy of Carbon Nanotubes, *Phys. Rep.*, 2004, **409**, 47–99.
 - 44 F. Liu, Z. Cao, C. Tang, L. Chen and Z. Wang, Ultrathin Diamond-Like Carbon Film Coated Silver Nanoparticles-Based Substrates for Surface-Enhanced Raman Spectroscopy, *ACS Nano*, 2010, **4**, 2643–2648.
 - 45 M. S. Dresselhaus, A. Jorio, M. Hofmann, G. Dresselhaus and R. Saito, Perspectives on Carbon Nanotubes and Graphene Raman Spectroscopy, *Nano Lett.*, 2010, **10**, 751–758.
 - 46 X. Zhang and R. Frech, Spectroscopic Investigation of $\text{Li}_{1+x}\text{V}_3\text{O}_8$, *Electrochim. Acta*, 1998, **43**, 861–868.
 - 47 G. X. Wang, S. Zhong, D. H. Bradhurst, S. X. Dou and H. K. Liu, Synthesis and Characterization of LiNiO_2 Compounds as Cathodes for Rechargeable Lithium Batteries, *J. Power Sources*, 1998, **76**, 141–146.
 - 48 W. Li, J. N. Reimers and J. R. Dahn, In situ X-Ray-Diffraction and Electrochemical Studies of $\text{Li}_{1-x}\text{NiO}_2$, *Solid State Ionics*, 1993, **67**, 123–130.
 - 49 E. Zhecheva and R. Stoyanova, Stabilization of The Layered Crystal-Structure of LiNiO_2 by Substitution, *Solid State Ionics*, 1993, **66**, 143–149.
 - 50 J. Xu, H. Zhang, T. Zhang, Q. Pan and Y. Gui, Influence of Heat-Treatment Temperature on Crystal Structure, Morphology and Electrochemical Properties of LiV_3O_8 Prepared by Hydrothermal Reaction, *J. Alloys Compd.*, 2007, **467**, 327–331.